Energy & Environmental Science

ROYAL SOCIETY OF CHEMISTRY

PAPER

View Article Online
View Journal | View Issue

Cite this: *Energy Environ. Sci.*, 2024, **17**, 6291

Enhanced polysulfide trapping in Li–S batteries by dipole alignment in ferroelectric $BaTiO_3$†

Jinglin Jiang,[a] Jorge Ontaneda,[b] Subhajit Pal,[b] Zhenyu Guo,[a] Chloe Forrester,[b] Kaitian Zheng,[ac] Mengnan Wang,[a] Joe Briscoe,*[b] Maria-Magdalena Titirici*[a] and Heather Au*[a]

Lithium sulfur (Li–S) batteries are a promising technology due to their high energy density and low cost. However, the polysulfide shuttle effect remains a significant cause of degradation in Li–S batteries and there is an urgent need for improved cathode materials that can effectively trap polysulfides to minimize this phenomenon. In this work, we propose a $BaTiO_3$ (BTO) cathode with controlled dipole alignment as a ferroelectric additive to improve polysulfide trapping. To evaluate the polysulfide adsorption on BTO with different degrees of dipole alignments, *operando* ultraviolet-visible diffuse reflectance spectroscopy (UV-vis DRS) and optical microscopy were used to track the shuttling of polysulfides in cycling Li–S batteries. The poled BTO cathodes demonstrated not only superior initial capacity, but also lower concentrations of shuttling polysulfides during cycling, resulting in a 24% improvement in capacity after 500 cycles as compared with the unpoled material. These improvements were attributed to the relatively strong electrostatic field induced by the highly aligned dipoles on the poled BTO surface, confirmed by X-ray photoelectron spectroscopy (XPS), Raman spectroscopy and density functional theory (DFT) modelling. We thus demonstrate, for the first time, the beneficial role of bulk aligned dipoles in ferroelectric materials for the suppression of polysulfide shuttling, and the resulting superior long-term cycling performance.

Received 3rd May 2024,
Accepted 22nd July 2024

DOI: 10.1039/d4ee01936a

rsc.li/ees

Broader context

Lithium–sulfur (Li–S) batteries are considered a promising option for next-generation energy storage systems due to their superior theoretical capacity (1675 mA h g^{-1}). However, their practical energy density and cycle life have not met expectations due to the shuttle effect, where polysulfides, as intermediate products, dissolve and migrate towards the lithium anode. This shuttle effect results in the loss of sulfur active materials and subsequent degradation of battery performance. To address this issue, we have integrated a ferroelectric $BaTiO_3$ additive with dipole alignment into the cathode, exploiting its ferroelectric properties to adsorb polysulfides on the sulfur cathode, thereby mitigating the shuttle effect and enhancing battery performance. We have explored the relationship between the degree of dipole alignment in the ferroelectric $BaTiO_3$ and its effectiveness in polysulfide adsorption. Our research indicates that high dipole alignment correlates with increased surface potential, leading to effective polysulfide adsorption, thus significantly suppressing the shuttle effect and improving long-term battery performance.

Introduction

In recent years, significant focus has been placed on the development of lithium–sulfur (Li–S) batteries, which offer a high theoretical capacity (1675 mA h g^{-1}) and energy density (2576 W h kg^{-1}), as well as substituting critical metals for abundant sulfur at the cathode.[1,2] Despite these merits, the commercialization of Li–S batteries has been hindered by the rapid decay in capacity arising from the polysulfide shuttle effect. This phenomenon is induced by the dissolution of intermediate polysulfides (Li_2S_x, $4 \leq x \leq 8$) into the electrolyte, and their unregulated deposition within the battery, which results in the loss of active sulfur, anode corrosion, and reduced coulombic efficiency. To address the challenge of polysulfide shuttling in Li–S batteries, several approaches have been developed, primarily categorized as pore encapsulation and chemical adsorption strategies. Porous carbon materials have been widely employed in Li–S batteries to enhance conductivity and trap polysulfides within the pores.[3] In addition,

[a] *Department of Chemical Engineering, Imperial College London, London, SW7 2AZ, UK. E-mail: h.au13@imperial.ac.uk, m.titirici@imperial.ac.uk*
[b] *School of Engineering and Materials Science, Queen Mary University of London, London, E1 4NS, UK. E-mail: j.briscoe@qmul.ac.uk*
[c] *Chemical Engineering Research Center, State Key Laboratory of Chemical Engineering, School of Chemical Engineering and Technology, Tianjin University, Tianjin 300072, China*

† Electronic supplementary information (ESI) available. See DOI: https://doi.org/10.1039/d4ee01936a

defects and heteroatoms in porous carbon materials permit the chemical adsorption of polysulfides,[4,5] although the adsorption efficiency of this method remains limited. Alternatively, chemical adsorption of polysulfides can be achieved through the use of polar metal-base additives in cathodes, including metal oxides,[6–8] metal sulfides[9,10] and metal organic frameworks.[11,12] As these metal-based additives are often poorly conductive, a strategy combining porous carbons with metal-base additives is typically employed in Li–S batteries.

Ferroelectric materials have a unique property of reversible self-polarisation where the orientation of the dipoles can be switched by applying an external electric field.[13] These dipoles provide polar surfaces and local electrostatic fields beneficial for polysulfide adsorption, contributing to the suppression of the shuttle effect.[14] $BaTiO_3$ (BTO), one of the most-studied perovskite-type ferroelectric materials, has previously demonstrated the ability to trap polysulfides and improve battery performance.[14–16] However, the ferroelectric materials utilised in previous Li–S studies were not polarised and possessed a random distribution of dipole orientations, which could result in an overall weak electrostatic field on the surface.[14–16] It is expected that polysulfide adsorption will be more efficient in poled ferroelectric materials due to the stronger local electrostatic fields of aligned dipoles compared to those with random alignment. In addition, these previous studies did not compare ferroelectrics with a non-ferroelectric analogue, thus not clearly differentiating ferroelectric contributions from those found in typical metal oxides.[14–16] It therefore remains unclear how ferroelectric polarisation in the cathode affects polysulfide adsorption.

In this work, a new approach employing a highly dipole-aligned ferroelectric material – poled BTO – as a cathode additive in Li–S batteries was explored for the first time (Fig. 1(a)). To investigate the effect of varying degrees of dipole alignment, three cathodes of poled BTO, unpoled BTO and non-ferroelectric $SrTiO_3$ (STO) were prepared and their performance evaluated (Fig. 1c). In the tetragonal phase of BTO, *z*-axis distortion of the Ti atom results in non-overlapping charge centres and self-polarization property (Fig. 1(b)). This distortion is not present in non-ferroelectric STO, allowing a direct comparison to demonstrate the unique ferroelectric effects of BTO in Li–S batteries. The BTO and STO nanoparticles were synthesised *via* a molten salt method and the electrodes were subsequently polarised using a corona poling technique. Piezoresponse force microscopy (PFM) was used to characterise the ferroelectric dipole alignment. In addition, an *operando* ultraviolet-visible diffuse reflectance spectroscopy (UV-vis DRS) technique was developed to monitor the change in polysulfide concentrations in cycling coin cells, allowing us to correlate the various dipole alignment states with the polysulfide adsorption behaviour. Overall, the cathode with poled BTO exhibited the most efficient polysulfide adsorption and superior battery performance, indicating that the alignment of dipole orientations is the most important factor determining the performance of ferroelectric materials as Li–S cathodes.

Results

Molten salt synthesis of $BaTiO_3$ and $SrTiO_3$ nanoparticles

A molten-salt synthesis method was employed to produce ferroelectric BTO from BaC_2O_4 and TiO_2 (Fig. 2(a)).[17] The molten-salt synthesis method is favoured over conventional

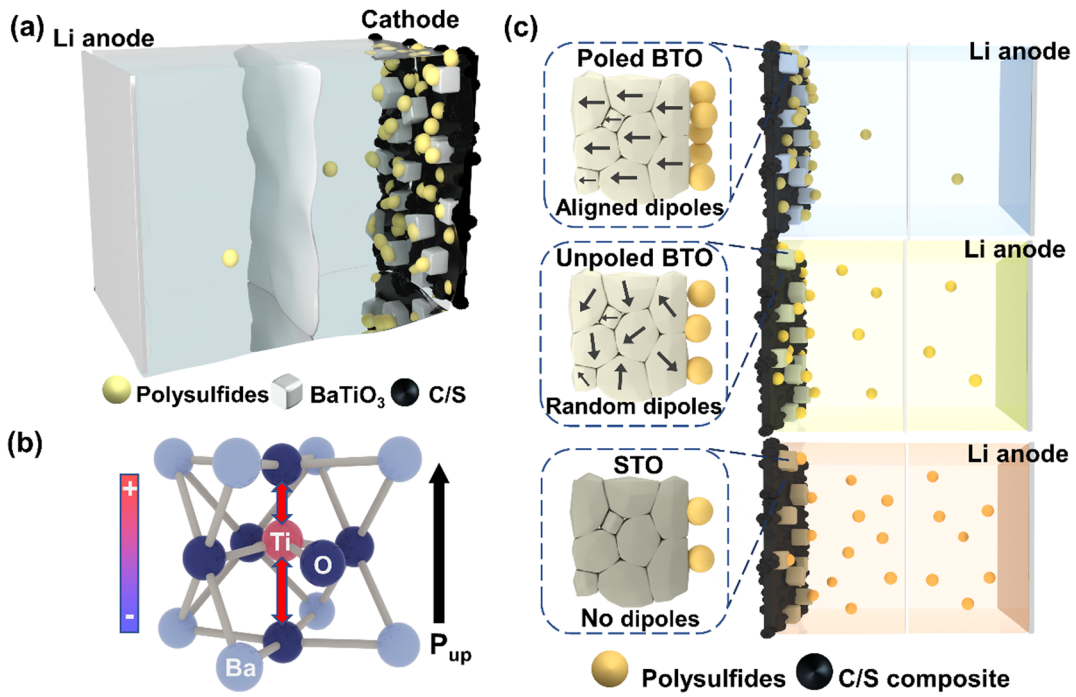

Fig. 1 Schematic illustrations of $BaTiO_3$ nanoparticles in Li–S batteries. (a) A Li–S battery with a composite ferroelectric $BaTiO_3$/C/S cathode; (b) a ferroelectric BTO lattice with upward polarisation; (c) polysulfide adsorption on cathodes of poled BTO, unpoled BTO and non-ferroelectric STO.

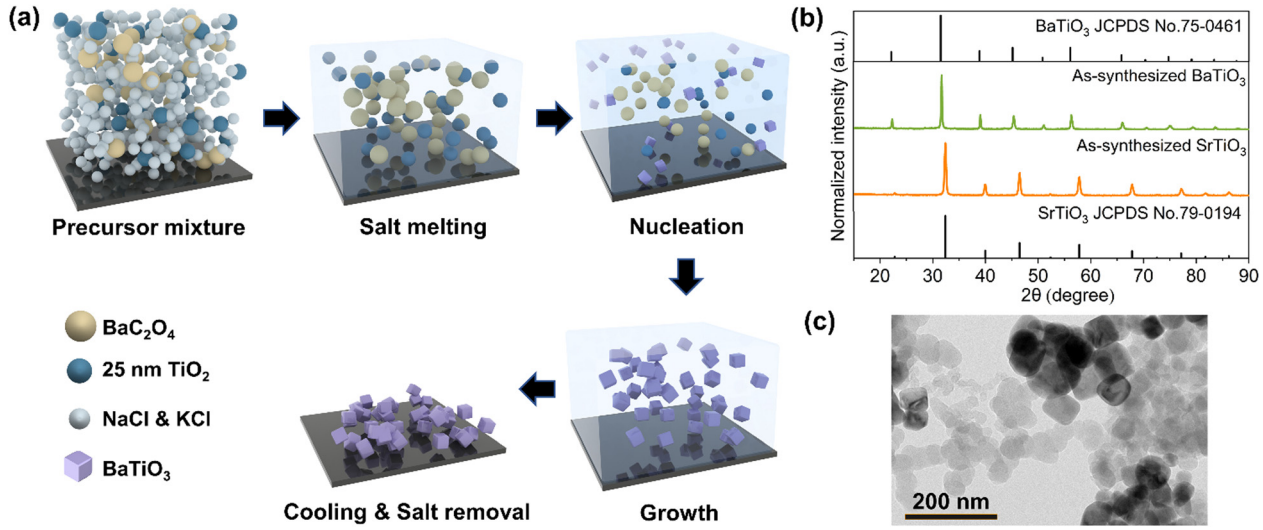

Fig. 2 Molten salt synthesis of $BaTiO_3$. (a) Molten salt synthesis process for ferroelectric BTO nanoparticles: the BaC_2O_4 and TiO_2 precursors were mixed with NaCl and KCl, heated to 750 °C with a heating rate of 1 °C min^{-1} then held for 1 h; the salt was removed by washing with warm deionised water; (b) XRD patterns of as-synthesised BTO and STO nanoparticles (CuKα 1.54 Å); (c) TEM image of the electrode slurry mix containing BTO nanoparticles, Super P carbon, and PVDF binder.

solid-state synthesis,[18] requiring a lower reaction temperature (750 °C). Additionally, the precursors are generally dispersed in molten NaCl and KCl, which regulates the reaction rate in order to produce nanoscaled BTO. STO nanoparticles were synthesized by the same method using SrC_2O_4 and TiO_2 as precursors. X-ray diffraction (XRD) patterns of the as-synthesized BTO and STO nanoparticles (Fig. 2(b) and Fig. S1, ESI†) confirm the presence of the ferroelectric tetragonal phase of BTO, whereas STO exists in the non-ferroelectric cubic phase. The BTO and STO nanoparticles were subsequently mixed with Super P carbon and polyvinylidene fluoride (PVDF) binder to test as cathodes in Li–S batteries. Transmission electron microscopy (TEM) (Fig. 2(c)) of the electrode slurry mixture showed the presence of BTO nanoparticles of uniform shape with diameters of approximately 80–150 nm. The uniformity of the particle size allowed smooth electrode coatings with homogeneous surfaces, as observed by scanning electron microscopy (SEM) (Fig. S2(a)–(d), ESI†).

Alignment and characterisation of dipole orientations

In a ferroelectric material, all ferroelectric dipoles in a ferroelectric domain have the same polarisation orientation. In the as-synthesised BTO nanoparticles, the domain orientations are likely randomly distributed, and therefore the overall alignment of ferroelectric dipoles may be poor (Fig. 1(c)). Domains with aligned orientations create increased localised electrostatic fields, which could be beneficial for polysulfide adsorption (Fig. 1(c)). We therefore carried out a corona poling process[19] (Fig. S3(a), ESI†) to align the polarisation orientations of BTO dipoles throughout the whole electrode (Fig. 3(a)). The corona poling setup consists of a saw electrode placed above a plate electrode on a hot plate (Fig. S3(a), ESI†). In order to switch the dipoles, the BTO electrode was heated to 150 °C, which is above the Curie temperature of BTO (120 °C). A positive high voltage of 7.5 kV was then applied to ionize the air in the surrounding atmosphere, allowing ions to migrate to the surface of the BTO electrode, facilitating the switching and alignment of all ferroelectric dipoles. Finally, the poled BTO electrode was cooled down to room temperature with the electric field maintained. To further investigate the ferroelectric effect in Li–S batteries, a negative voltage of 7.5 kV was also applied on the saw electrode to align the BTO dipoles in the other direction, obtaining the reverse-poled BTO electrode.

To characterise the ferroelectric domains following corona poling, Kelvin probe force microscopy (KPFM) and piezoresponse force microscopy (PFM) techniques were applied to both poled and unpoled BTO electrodes (Fig. 3(b)–(g)). The PFM phase and amplitude hysteresis loops (Fig. 3(b) and (c)) suggest that both the poled and unpoled electrodes present ferroelectric responses to the applied voltage. However, the dipole orientation (Fig. 3(f)), determined from the PFM phase measurements (Fig. 3(d) and (e)), shows a marked change in distribution following corona poling. Prior to poling, the unpoled BTO electrode exhibited random dipole alignment with both up and down orientations (bright and dark contrast in Fig. 3(d), respectively). After poling, the electrode exhibited only down-oriented dipoles (Fig. 3(f)), indicating that the corona poling process successfully aligned the BTO dipoles. Moreover, the overall surface potentials are higher (Fig. 3(g)), determined from the KPFM measurements (Fig. S3(d) and (e), ESI†), demonstrating a 300 mV stronger surface electrostatic field on the poled BTO electrode after poling. However, the polyvinylidene fluoride (PVDF) binder is a recognised ferroelectric material in its β phase,[20] and might also be polarised during the corona poling process. Therefore, to determine whether this corona poling process affected the properties of the PVDF, a poled STO electrode was fabricated using the same method as the poled BTO electrodes. PFM phase measurements

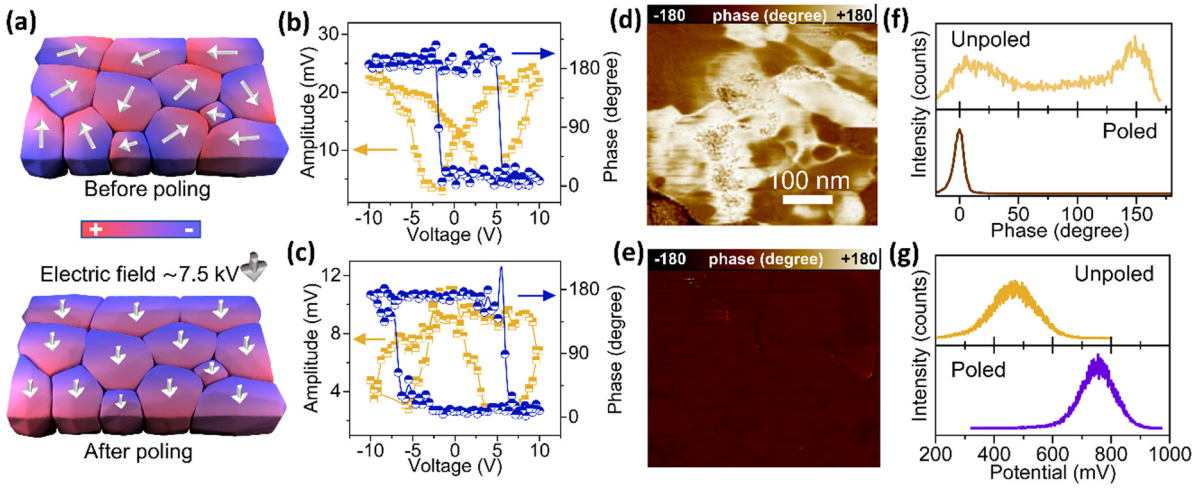

Fig. 3 Ferroelectric properties of $BaTiO_3$. A schematic illustration of ferroelectric dipoles before and after the poling process (a); phase and amplitude loops from PFM of the unpoled BTO (b) and poled BTO (c) electrodes, showing that both the poled and unpoled BTO exhibit a ferroelectric response; PFM surface potential images of the unpoled BTO (d) and poled BTO (e) electrodes; (f) the distribution of dipole orientations on the poled and unpoled BTO electrodes, obtained from Fig. 3(d) and (e); (g) the distribution of surface potentials of poled and unpoled BTO electrodes, obtained from Fig. S3(d) and (e) (ESI†).

(Fig. S3(b) and (c), ESI†) demonstrate that neither the unpoled nor poled STO electrodes exhibited any ferroelectric response, confirming that the corona poling technique did not change PVDF into its ferroelectric β phase. We can thus conclude that the enhanced surface electrostatic field in the BTO electrode is due to the alignment of the BTO dipoles.

Electrochemical performance

To investigate their performance as cathodes, Li–S coin cells were assembled with the poled and unpoled BTO or STO cathodes, against a Li metal anode. The conventional method of introducing sulfur to the cathode by melt infiltration is not suitable for BTO electrodes, because the melt infiltration temperature of 155 °C exceeds the Curie temperature of BTO (120 °C) and would thus induce phase changes in BTO and loss of ferroelectric polarisation. Instead, sulfur infiltration was achieved by dropping a 0.2 M Li_2S_8 solution onto the cathodes. Prior to cycling, the cells underwent an activation step of a C/10 charge to 2.8 V (we take a rate of 1C to be a current density of 1675 mA g^{-1}), followed by a 4-hour constant voltage charge (CVC) at 2.8 V, to ensure complete conversion of Li_2S_8 into solid sulfur. The cells were then cycled galvanostatically between C/10 and 1C. Both poled BTO and unpoled BTO exhibited two reduction plateaus at approximately 2.3 and 2.1 V at each C-rate, representing the two-step reduction process of sulfur (Fig. 4(a) and Fig. S4, ESI†).[21] The poled and reverse-poled BTO achieved the highest first-cycle capacities of 1379 mA h g^{-1} and 1368 mA h g^{-1} at C/10, while the unpoled BTO exhibited a first-cycle capacity of 1250 mA h g^{-1}. These values are far higher than the initial capacities achieved in the poled STO (925 mA h g^{-1}) and unpoled STO electrodes (862 mA h g^{-1}), suggesting that the presence of ferroelectric dipoles in the BTO electrodes is beneficial for electrochemical performance. Moreover, the poled BTO electrode with the highest dipole alignment retains the highest specific capacity at each C-rate (Fig. 4(b)). Indeed, as the C-rate increases, the capacity difference between

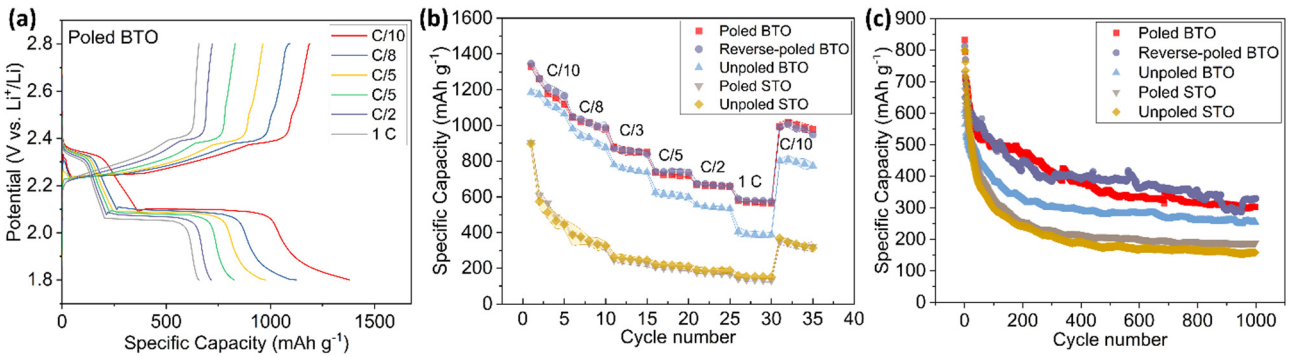

Fig. 4 Electrochemical performance of the $BaTiO_3$ electrodes. (a) Galvanostatic discharge–charge curves at varying C-rates of the cell with poled BTO electrode; (b) comparison of C-rate performance from C/10 to 1C, then 5 cycles at C/10; (c) long cycle performance at 1C for the poled, reverse-poled and unpoled BTO, and poled and unpoled STO electrodes; a rate of 1C is a current density of 1675 mA g^{-1}.

poled and unpoled BTO electrodes increases. In contrast, there is little variation between the poled and unpoled STO electrodes, confirming that the poling process had no effect on the non-ferroelectric material. Furthermore, the poled BTO showed the greatest recovery after C-rate testing, when returning to C/10 cycling (Fig. 4(b)). Longer cyclic testing at 1C was subsequently undertaken, with the poled and reverse-poled BTO electrodes exhibiting the best cyclic performance among the tested samples (Fig. 4(c)); the sudden capacity fluctuations were caused by brief power outages. The discharge capacities after 200 cycles at 1C for poled BTO, reverse-poled BTO, unpoled BTO, and unpoled STO are 469, 457, 330, and 255 mA h g^{-1}, respectively; after 500 cycles, the retained capacities are 351, 386, 283, and 207 mA h g^{-1}, respectively. These results from galvanostatic cycling suggest that the electrochemical performance is highly dependent on the dipole alignment within the cathode. All BTO electrodes outperform the STO cathodes, which lack any dipole, while the high dipole alignment in the poled and reverse-poled BTO electrodes are beneficial for C-rate performance, and especially for long cycle stability. Indeed, a cycled poled electrode after 600 cycles at 1C showed the dipoles still retain a relatively high degree of alignment (Fig. S5, ESI†). Although the distribution of dipole orientations after long cycles is slightly wider than for the pristine poled electrode, owing to interactions between the BTO surface and adsorbed polysulfides, the cycled poled BTO still maintained a high degree of dipole alignment. Notably, both the poled and reverse-poled BTO exhibited similar battery performance, suggesting that the degree of dipole alignment is the main influencing factor rather than the specific poling direction.

Operando measurements and evaluation of polysulfide adsorption

This improved battery performance is likely attributed to the strong polysulfide adsorption arising from the high alignment of dipoles. It has previously been reported that ferroelectric materials are able to adsorb polysulfides, although these studies only considered unpoled materials and did not compare to a non-ferroelectric analogue.[22–24] We thus employed *operando* ultraviolet-visible diffuse reflectance spectroscopy (UV-vis DRS) to track shuttling polysulfides in Li–S coin cells undergoing cycling (Fig. 5(a) and Fig. S6(a), ESI†), in order to evaluate the polysulfide adsorption ability of materials with different degrees of dipole alignment. The cell setup allows detection of polysulfide signals on the separator close to the Li anode side, which corresponds to the dissolved polysulfides that have shuttled away from the cathode and across the separator. Following calibration[25–27] to confirm specific absorption wavelengths for Li_2S_6 and Li_2S_8 and allow quantitative analysis (see Fig. S7 and Experimental section for more details, ESI†), the concentration of these polysulfides on the separator may be correlated to the adsorption ability of the ferroelectric cathode additives, and thus related to the overall cycling behaviour observed for each material. Li_2S_4 and Li_2S_2 were not measured due to their low solubility and the incomplete dissolution of Li_2S and S.

Each coin cell underwent 3 cycles at C/6 while UV-vis reflectance spectra were collected at 10-minute intervals (Fig. S6(b), ESI†). In the first discharge plateau of the poled BTO electrode, solid sulfur is converted into soluble long-chain polysulfides, leading to a rapid increase in the concentrations of Li_2S_8 and Li_2S_6 (Fig. 5(b) and Fig. S8(a), ESI†). A

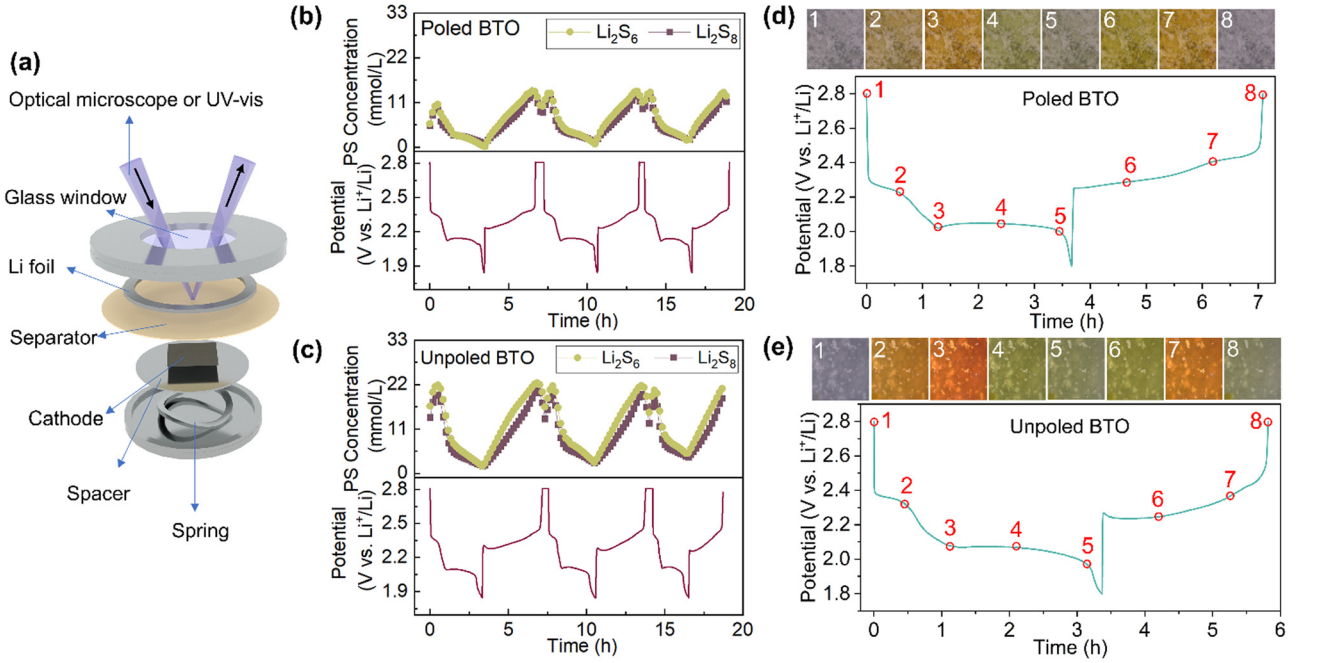

Fig. 5 *Operando* UV-vis DRS and optical microscope measurements of a Li–S cell with $BaTiO_3$ cathodes. (a) Configuration of the *operando* Li–S coin cell; (b) and (c) variation in polysulfide concentration on the separator with galvanostatic cycling, determined by UV-vis, for cells containing the poled BTO (b) and unpoled BTO (c) electrodes; (d) and (e) optical images of the separator at different stages of discharge/charge, and the corresponding 1st cycle galvanostatic curves at C/6 of poled BTO (d) and unpoled BTO (e).

corresponding increase in the cell overpotential is observed during the galvanostatic intermittent titration technique (GITT) (Fig. S9(c), ESI†), in which a pulsed current sequence is performed, and the iR drop (overpotential) between the equilibrium potential and current-on potential allows us to evaluate the electrochemical polarisation within the battery.[28] After the first plateau, an increase in the cell overpotentials indicates an increased viscosity of the electrolyte arising from the high concentration of shuttling polysulfides, potentially leading to sluggish ion kinetics.[29] As these species convert to Li_2S_4 by $\sim$2.05 V, the measured concentration of long-chain polysulfides decreases correspondingly. In the second discharge plateau, the electrochemical reaction of Li_2S_4 to Li_2S occurs in parallel to the continued conversion of Li_2S_8 and Li_2S_6 to Li_2S_4. Under galvanostatic testing conditions, consumption of Li_2S_8 and Li_2S_6 therefore slows down, corresponding to a continued decrease in concentration but at a slower rate (Fig. S8(a), ESI†). The lowest Li_2S_8 and Li_2S_6 concentrations occur once full discharge is reached, correlating to the rapidly increased overpotentials near the end of discharge in GITT (Fig. S9(c), ESI†), as expected due to the depletion of reactants. The unpoled BTO and STO electrodes (Fig. 5(c) and Fig. S8(b) and (c), ESI†) exhibit a two-step behaviour during discharge similar to the poled BTO electrode, consistent with their similar charge–discharge voltage profiles. Upon charging, following the initial overpotential at around 2.3 V related to the conversion of Li_2S into soluble polysulfides,[21,30] the concentration of shuttled polysulfides increases steadily (Fig. S8(a), ESI†) in all electrodes, before decreasing rapidly at the end of charge. These results are consistent with the conversion of Li_2S into soluble polysulfides as the voltage increases, before depositing solid sulfur at the final stage of charging.

Optical microscopy provides a simple, visual corroboration of the changing concentration of polysulfides on the separator during cycling, and qualitative comparison between the polysulfide adsorption abilities of the poled and unpoled BTO electrodes (Fig. 5(d) and (e)). It can clearly be seen that the overall polysulfide concentrations at all stages in the first 3 cycles were lowest in the poled BTO (Fig. 5(b)), while the unpoled STO had the highest concentrations of Li_2S_6 and Li_2S_8 (Fig. S8(c), ESI†). Notably, unpoled BTO (Fig. 5(c)) exhibited peak concentrations that were only slightly lower than those of poled and unpoled STO (Fig. S8(b) and (c), ESI†), but significantly higher than those of the poled BTO. Hence, while the dipoles of the unpoled BTO electrode appear to facilitate stronger polysulfide adsorption than the dipole-free STO, the random alignment of dipoles in unpoled BTO still results in an overall weakly localised electrostatic field and thus minimal improvement in adsorption. In contrast, the aligned dipoles of the poled BTO electrode exert a strong and uniform localised electrostatic field on the surface, leading to the strongest polysulfide adsorption and the lowest degree of polysulfide shuttling in the cell. A consequence of this strong polysulfide adsorption was observed during GITT (Fig. S9(c), ESI†), where the overpotential of the poled BTO is lower than the unpoled BTO throughout the whole cycle, especially between the two discharge plateaus with the most shuttling polysulfides. The calculated polysulfide concentrations for poled STO (Fig. S8(b), ESI†) were similar to those in the unpoled STO (Fig. S8(c), ESI†), indicating that the corona poling only induced noticeable changes in BTO. These observations suggest that the net dipole alignment of ferroelectrics plays a crucial role in suppressing polysulfide adsorption and shuttle behaviours.

DFT modelling and characterisation of surface interactions

Adsorption of the polysulfides on the BTO surface was further explored with DFT calculations on two kinds of BTO crystalline planes: the (001) and (100) which are perpendicular and parallel to the Ti distortion, and were chosen to simulate the polar and non-polar surfaces, respectively (see ESI† and Experimental section for more details). The most stable adsorption complexes for Li_2S_6 and Li_2S_8 on BTO(001) and BTO(100) are presented in Fig. 6(a) and (b). Polysulfide adsorption was calculated to be exothermic in both cases, but is thermodynamically more favourable on the polar surface ($>$5.0 eV for BTO(001) *vs.* 1.3–1.6 eV for BTO(100)). Interestingly, the interaction between the Li of the adsorbate and the O atoms at the BTO surface is weaker at the polar BTO(001) surface, demonstrated by the longer Li–O bond lengths of 1.92 Å for Li_2S_6 and 1.86 Å for Li_2S_8, compared with 1.76 Å for both polysulfides on BTO(100). Instead, the greater adsorption strength of both polysulfide species on BTO(001) may be attributed to the formation of more Ba–S contact points on BTO(001) resulting in overall shorter Ba–S bond distances of 3.24–3.60 Å compared with 3.50–3.66 Å on the non-polar surface. The formation of these Ba–S contact points is likely due to the effect of ferroelectric polarization along the (001) axis in the BTO unit cell.

These interactions were observed experimentally by Raman and XPS measurements of the cathodes after the first cycle at C/10 (Fig. 6(c)–(e)). In the Raman spectra (Fig. 6(c)), the S_8 peaks at 152, 218 and 472 cm^{-1} were observed on all samples: cycled poled and unpoled BTO, and pristine sulfur powder. However, an additional peak of 460 cm^{-1} was observed only on the cycled poled BTO electrode, corresponding to the interaction between Ba and S.[31] We also observed these interactions with XPS employing Ar etching to investigate composition at different depths. The doublet peak attributed to $BaTiO_3$ (780.4 and 795.6 eV) was detected on the surface of the unpoled, poled and reversed-poled BTO electrodes (Fig. 6(d) and (e) and Fig. S10(a), ESI†); the intensity and peak position remaining stable during etching (Fig. 6(e) and Fig. S10(c), ESI†), indicating no significant impact on the surface chemistry of Ba by the etching ion beam. An additional doublet peak was only identified on the cycled poled and reverse-poled BTO electrodes, with a shift of 1.2–1.4 eV to a lower binding energy (Fig. 6(d) and Fig. S10(a), ESI†); this downshift in binding energy has previously been reported as corresponding to a Ba–S bond.[32] This observation is in agreement with our DFT calculations which also show a greater average Ba 3d downshift on the polar surface, BTO (001) (Fig. 6(f) and Table S1, ESI†). For each Ba atom in these 4 polysulfide-BTO adsorption complexes in Fig. 6(a) and (b), the simulated Ba 3d peak shows a contribution from two groups

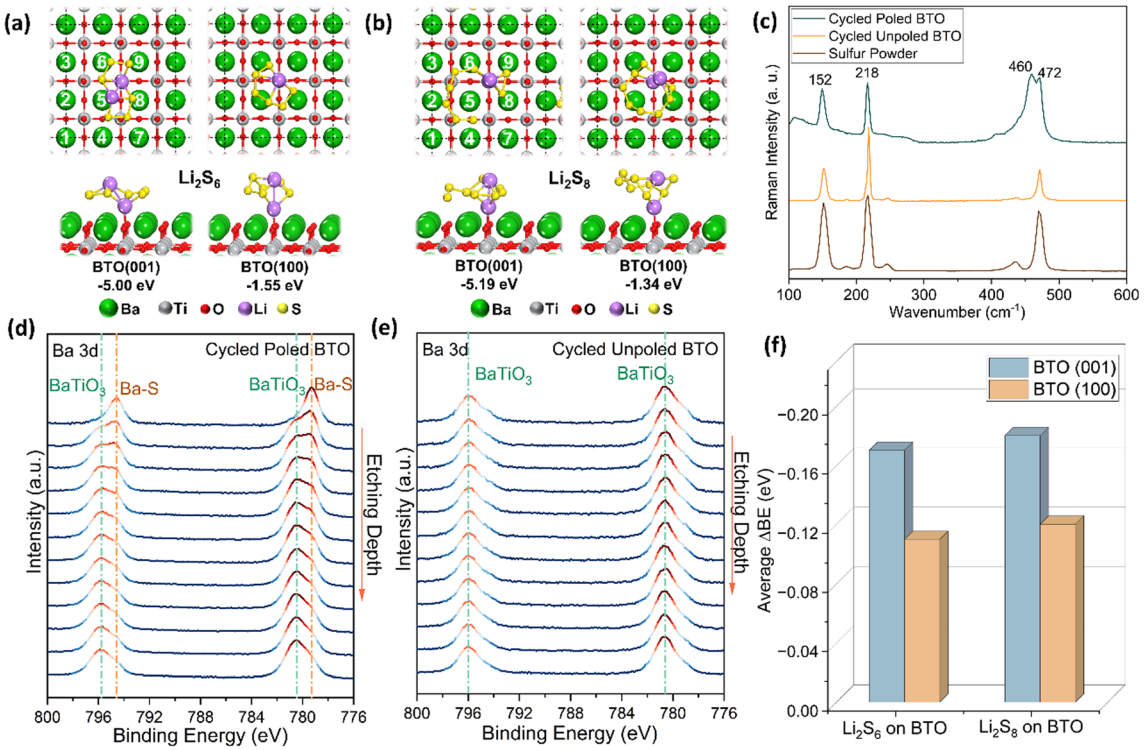

Fig. 6 Surface characterisations and DFT simulations of polysulfide adsorption on $BaTiO_3$. DFT calculations of the lowest-energy configurations of adsorption of (a) Li_2S_6 and (b) Li_2S_8 on BTO(001) and BTO(100) surfaces, with Ba atoms numbered in line with Table S1 (ESI†); (c) Raman spectra of poled and unpoled BTO electrodes after 1 cycle at C/10, and pristine sulfur powder; (d) Ba 3d XPS depth profile of a poled BTO electrode after 1 cycle at C/10; (e) Ba 3d XPS depth profile of an unpoled electrode after 1 cycle at C/10; (f) simulated average Ba 3d binding energies of Li_2S_6 and Li_2S_8 on BTO (001) and (100), with values given in Table S1 (ESI†).

(Fig. S11(a)–(d) and Table S1, ESI†). The lower binding energy environment corresponds to surface Ba atoms interacting with S atoms of the Li_2S_6 or Li_2S_8 molecule, while the second group at higher binding energy corresponds to non-interacting Ba atoms. The discrepancy between the magnitude of the simulated and measured binding energy shifts may arise because the DFT models considered only perfect surfaces, and the core screening effects were neglected, but the trend towards a greater shift on the polar surface is consistent with experimental observations (Fig. 6(d) and (e)). As the etching depth increases during XPS acquisition, the normalised intensity of the Ba–S peaks on poled and reverse-poled BTO decreases, confirming that binding between Ba and S is predominantly on the surface (Fig. S10(b) and (c), ESI†). These observations suggest that the poled and reverse-poled BTO surface with highly-aligned ferroelectric dipoles facilitate the formation of stronger Ba–S bonds, in line with our DFT calculations, which effectively anchor polysulfides onto the cathode. These stronger Ba–S bonds of the poled BTO result in far lower impedance than the unpoled BTO (Fig. S9(d), ESI†), suggesting faster charge transfer on the poled BTO electrode. This additional anchoring also allows better retention of polysulfides upon repeated cycling, resulting in lower capacity fade compared to the unpoled electrode (Fig. 4(c)).

Overall, ferroelectric materials have been suggested as an effective cathode additive for polysulfide adsorption, but previously the effect of poling on Li–S cathodes has not been studied. Here we show that it is the degree of dipole alignment in the whole electrode that is critical for polysulfide adsorption, as demonstrated by *ex situ* XPS, Raman, *operando* UV-vis and optical microscope techniques, including the Ba–S bonding found in XPS and Raman results. The similar performance of poled and reverse-poled BTO electrode shows different orientations of dipole alignment have the same effect on polysulfide adsorption and battery performance, suggesting these improvements are mainly attributed to the strong localised electrostatic field from the aligned ferroelectric dipoles throughout the whole electrode.

Conclusions

In summary, we have demonstrated the ferroelectric effects on the performance of Li–S cathodes with a modified degree of dipole alignment *via* poling, and elucidated the mechanisms underlying these behaviours. Ferroelectric BTO nanoparticles were synthesised by the molten salt method, and a subsequent corona poling process was used to produce electrodes containing dipoles with aligned orientations. The dipole alignment of the poled BTO electrodes was confirmed by PFM. When tested as a cathode in a Li–S coin cell, these electrodes exhibited superior long-term cycling and rate capability compared with

unpoled BTO and STO electrodes, which we attribute to the improved polysulfide retention due to the stronger localised electrostatic field from the aligned dipoles. The changing concentration of shuttling polysulfides during galvanostatic cycling was quantified by *operando* optical microscope and UV-vis DRS measurements; the concentration of long-chain polysulfides was lowest in the cell with the poled BTO electrode, suggesting that greater polysulfide retention occurred in the material with greatest dipole alignment. These conclusions were supported by results from XPS and DFT modelling, which confirmed that the poled BTO electrode surface with aligned dipoles is highly beneficial for polysulfide adsorption by favouring Ba–S bonds at the surface. Interestingly, the comparison between poled and reverse-poled BTO suggested that the direction of bulk alignment does not affect polysulfide adsorption ability. Overall, this work demonstrated that it is not only the presence of dipoles in BTO, but crucially, their strong localised electrostatic field from high degree of alignment that enhances polysulfide adsorption, reduces the shuttle effect, and improves battery performance.

In this study, we used a simplified cathode system comprising $BaTiO_3$ and Super P to provide a proof of concept. To advance the discoveries of this work, it is important to optimise electrode components and fabrication methods, to exploit the beneficial properties of ferroelectrics in combination with enhanced host materials for BTO and sulfur, and ferroelectric materials with higher Curie temperature allowing the melt infiltration of sulfur. Overall, however, these materials demonstrate the highly beneficial effect of a localised electrostatic field on polysulfide adsorption, and represent a promising development towards achieving stable, high-capacity cathodes for Li–S batteries.

Experimental section

Materials

Polyvinylidene fluoride (PVDF, average $M_w \sim 534\,000$ by gel permeation chromatography, powder) was purchased from Merck. *N*-Methyl-2-pyrrolidone (NMP), dimethyl ether (DME), dioxolane (DOL), lithium bis(trifluoromethanesulfonyl)imide (LiTFSI, 99.95%), lithium nitrate (99.999%), Super P conductive carbon (99%), lithium sulfide (99.98%), sulfur powder (99.98%), silver nitrate (99%) and titanium dioxide (TiO_2, P25 21 nm, 99.5%) were purchased from Sigma Aldrich. Strontium oxalate (95%), barium oxalate (99.999%), sodium chloride (99.999%) and potassium chloride (99%) were purchased from Alfa Aesar. The chemicals were used as received without further purification. CR2032 coin cells were purchased from Guangdong Canrd New Energy Technology Ltd.

Molten salt synthesis for $BaTiO_3$ or $SrTiO_3$

The precursors (BaC_2O_4/SrC_2O_4 and TiO_2, 1 : 1 molar ratio, 0.007 mol) were mixed to form a thin slurry with ethanol. This slurry was further mixed in a planetary ball mill for 4 h at 300 rpm then dried at 100 °C in air overnight. The mixed precursor powder was ground together with a mixture of NaCl and KCl (1 : 1 mole ratio). The mole ratio of precursor to salt is 1 : 30. This mixture was heated in an alumina crucible to 750 °C in air at 1 °C min^{-1} and held for 1 h. After cooling the mixture to room temperature, warm deionised water was used to dissolve and remove the remaining salt. A planetary centrifuge was used multiple times to remove all the remaining salt, confirmed with the addition of $AgNO_3$ solution. The final product was rinse with ethanol and dried overnight at 80 °C.

Preparation of electrodes

A slurry solution of 45 wt% $BaTiO_3$ or $SrTiO_3$ (molten salt synthesis), 45 wt% Super P and 10 wt% PVDF was stirred with a mortar and pestle for 30 min with sufficient NMP to achieve a smooth dropping consistency. This mixed slurry was then coated on 16 μm Al foil by a doctor blade (200 μm in thickness), then dried overnight at 80 °C. The dried foils were cut into square, 8 mm × 8 mm electrodes.

Corona poling and ferroelectric measurements

A lab-made corona poling setup was employed to align the ferroelectric dipoles of $BaTiO_3$. This corona poling setup consists of a saw electrode and a plate electrode. The plate electrode made of stainless steel is on a hot plate, grounded and connected to a high DC voltage supply. The distance between the plate and saw electrode is ~15 cm. The electrode foils were laid on the plate electrode and below the saw electrode, and heated over the Curie temperature (130 °C for $BaTiO_3$) before the poling process. A voltage of 7 kV was then applied across the two electrodes (positive voltage on the saw electrode). The saw electrode was moved horizontally every 30 min to enlarge the effective area of poling. The poled and unpoled electrodes were analysed with a Bruker PFM, with an amplitude of 2 V AC and 0.5 Hz.

Characterisation

SEM was performed on a FEI Inspect-F SEM at 10 kV. TEM was conducted on a JEOL 2100 Plus at 200 kV operating voltage. Raman spectroscopy was carried out with a Renishaw inVia Raman spectrometer using a 532 nm laser with 10% laser power and 1 s acquisition time. XRD was conducted on a X'Pert Pro X-ray diffractometer, with Cu Kα radiation (λ = 1.54 Å) at room temperature. XPS was performed using a ThermoFisher Nexsa X-ray spectrometer with an Al Ka X-ray source. The high resolution XPS spectra were collected with 50 eV pass energy and 0.1 eV step size. An argon ion beam was employed to obtain the XPS depth profile, with an etching energy of 500 eV and etching time of 20 s. The electrode samples for XPS and Raman were obtained after disassembling the cell after 1 cycle at 0.1C in the glovebox, and transferred to the spectrometer with a vacuum suitcase. PFM measurements were performed at contact resonance frequency using a Bruker Dimension icon with ScanAsyst AFM (Nanoscope-6). All PFM measurements were performed using SCM-PIT-V2 cantilever having a force constant of ~3 N m^{-1}. PFM measurements were performed in the capacitor geometry under sample bias conditions. PFM phase

and amplitude responses were extracted in the bias-off conditions using a Python script. KPFM measurements were carried out using the same cantilever used in PFM measurements.

Electrochemistry

The Li–S coin cells were assembled in an argon-filled glovebox (mBraun, $H_2O < 0.5$ ppm, $O_2 < 0.5$ ppm). DME and DOL were dried over 4 Å molecular sieves overnight, and subsequently mixed with a volume ratio of 1 : 1. $LiNO_3$ and LiTFSI were dried at 80 °C under vacuum overnight; to make the electrolyte, $LiNO_3$ and LiTFSI were added to DME/DOL solvent and stirred until fully dissolved, to obtain concentrations of 1 M LiTFSI and 0.8 M $LiNO_3$ in DME/DOL (1 : 1 v) electrolyte. A 0.2 M Li_2S_8 solution was prepared for easy addition of sulfur to the cathode, by combining stoichiometric amounts of Li_2S and S in DME/DOL solvent and stirring until fully dissolved. A metallic lithium foil (Goodfellow, 99.9%, 0.12 mm thickness, 12 mm diameter) was used as the anode against either a $BaTiO_3$ or $SrTiO_3$ cathode. To load the sulfur, 0.2 M Li_2S_8 solution was dropped onto the cathode then dried in the glovebox for 1 h before assembling the cell. The amount of solution was calculated based on a total sulfur loading of 50% of the electrode weight. The mass ratio of elemental sulfur to BTO is 4 : 3. The sulfur loading is about 0.5 mg(S) per cm^2. Celgard 2400 (Sigma) was used as the separator in the standard coin cells and Whatman GF/A glass microfiber (Sigma) was used in the *operando* cells. 50 μL electrolyte was added in each coin cell and 60 μL in each *operando* cell. All the assembled Li–S coin cells were charged to 2.8 V at 0.1C followed by a constant voltage charge (CVC) at 2.8 V for 2 h before conducting any electrochemical tests, to convert all the Li_2S_8 into elemental sulfur. Galvanostatic C-rate and cycling tests were performed on a LAND CT2001A battery testing system between 1.8 V and 2.8 V. Galvanostatic intermittent titration technique (GITT) was also conducted on a LAND CT2001A with 10-min charge or discharge interval and 60-min rest. The coin cells for GITT were discharged then charged for 1 cycle at C/10, between 1.8 V to 2.8 V. The electrochemical impedance spectroscopy (EIS) was conducted on a Biologic-VSP-300 workstation, with a frequency range from 0.01 Hz to 10^6 Hz.

Operando optical microscopy and *operando* UV-vis DRS spectroscopy

Operando optical microscopy was conducted on a Keyence VHX-7000 digital microscope with a portable Palmsens potentiostat. The optical *operando* coin cell was cycled at C/6 for 1 cycle.

The *operando* UV-vis measurements were conducted using a Shimadzu UV-2600 instrument with a reflectance kit. Wavelengths from 300 nm to 700 nm were used, and the scan interval was 0.5 nm. The scan speed was selected as ''medium''. The *operando* coin cells included a glass window on the shell and were assembled in a similar way to a normal coin cell, using instead a metallic lithium ring anode. The *operando* cell was connected to a portable Palmsens potentiostat to cycle at C/6 for 3 cycles. A CVC process at 2.8 V was applied at the end of charging to fully charge the cathode. UV-vis spectra were acquired at 10 min intervals during cell cycling. The standard UV-vis spectra of different polysulfides used for calibration were obtained from *operando* cells containing only Li_2S_6 or Li_2S_8. For these measurements, the anode and cathode in the cell were replaced by a 0.5 mm spacer to maintain the same pressure as a standard Li–S coin cell. Identical electrolytes were used, varying only the Li_2S_6 or Li_2S_8 concentrations between 0 and 20 mM, and the corresponding UV-vis spectra were collected.

The wavelength with the maximum value in the first derivative of the standard UV-vis spectra was used to confirm the range of specific absorption wavelengths of Li_2S_6 or Li_2S_8. Within this range, the wavelength with the highest linear correlation was chosen as the representative wavelength for that polysulfide. These specific wavelengths were used to calculate the concentration of shuttling polysulfides in the cycling cells.

Computational methods

The periodic DFT calculations were performed by means of the plane-wave code VASP,[33,34] using the projected augmented wave (PAW) method[35,36] to describe the interaction between core electrons and ions. The plane-wave basis set in the slab calculations was limited by a kinetic energy cutoff of 500 eV. Total energies were obtained using the generalized gradient approximation (GGA) in the form of the Perdew–Burke–Ernzerhof (PBE) exchange–correlation functional.[37] To partly counteract the artificial delocalization resulting from the spurious electron self-interaction in DFT,[38,39] we applied a Hubbard-type correction[40] to the Ti 3d orbitals with U_{eff} = 2.6 eV. For the Brillouin zone sampling, we employed Monkhorst–Pack grids[41] with a maximum separation of 0.25 $Å^{-1}$ between *k*-points. This grid density, which was found to be enough for convergence of the bulk BTO total energy, is equivalent to a 3 × 3 × 1 grid for the reciprocal space of the slab calculations. In our simulations, convergence during geometry optimizations was achieved when forces acting on ions were below 0.01 eV $Å^{-1}$.

Core-level shift calculations within the DFT+*U* method have been commonly used in the identification of surface adsorbates on transition metal oxides and assignment of their XPS peaks.[42] The *U* parameter works as a penalisation in the d–f orbitals of the transition metals, in order to correct the hybridisation with s orbitals. To achieve agreement between XPS and core-level shift calculations within the DFT+*U* approach it is suggested to adjust the choice of the *U* parameter in terms of surface-dependent properties such as SXRD and XPS.[43] However, in our DFT simulations the choice of *U* was based on a bulk property: spontaneous polarization (see ESI† for more details).

Author contributions

J. J. designed and performed the experimental work and wrote the manuscript. J. O. performed the computational work and contributed to writing the manuscript. S. P. conducted the dipole characterizations and discussed the results. Z. G. contributed to designing the *operando* measurements and discussion. C. F.

contributed to designing the corona poling setup. K. Z. discussed the results and contributed to the diagrams. M. W conducted the SEM and XRD. H. A. contributed to writing the manuscript and supervised the work. M. T. and J. B. supervised the work.

Data availability

Data for this article, including XRD, PFM, XPS, Raman, *operando* UV/vis and electrochemistry, are available at figshare at **https://figshare.com/s/ea0a4d5d1fc352234dbc**.

Conflicts of interest

The authors declare no competing interests.

Acknowledgements

The authors would like to thank the Faraday Institution's LiSTAR project (EP/S003053/1, grant FIRG014) for funding. HA acknowledges support from the Royal Society (URF/R1/231213). This project also received funding from the European Research Council (ERC) under the European Union's Horizon 2020 research and innovation programme (grant agreement no. 101001626).

References

1 Z. Pan, D. J. Brett, G. He and I. P. Parkin, Progress and perspectives of organosulfur for lithium–sulfur batteries, *Adv. Energy Mater.*, 2022, **12**, 2103483.
2 A. Manthiram, Y. Fu and Y.-S. Su, Challenges and prospects of lithium–sulfur batteries, *Acc. Chem. Res.*, 2013, **46**, 1125–1134.
3 N. Jayaprakash, J. Shen, S. S. Moganty, A. Corona and L. A. Archer, Porous hollow carbon@ sulfur composites for high-power lithium–sulfur batteries, *Angew. Chem.*, 2011, **123**, 6026–6030.
4 H. Ma, *et al.*, Defect-rich porous tubular graphitic carbon nitride with strong adsorption towards lithium polysulfides for high-performance lithium-sulfur batteries, *J. Mater. Sci. Technol.*, 2022, **115**, 140–147.
5 K. Liu, *et al.*, Hierarchical mesoporous heteroatom-doped carbon accelerating the adsorption and conversion of polysulfide for high performance Lithium–Sulfur batteries, *Compos. Commun.*, 2022, **30**, 101079.
6 Y. Zheng, *et al.*, A high-entropy metal oxide as chemical anchor of polysulfide for lithium-sulfur batteries, *Energy Storage Mater.*, 2019, **23**, 678–683.
7 X. Tao, *et al.*, Balancing surface adsorption and diffusion of lithium-polysulfides on nonconductive oxides for lithium–sulfur battery design, *Nat. Commun.*, 2016, **7**, 11203.
8 X. Liu, J. Q. Huang, Q. Zhang and L. Mai, Nanostructured metal oxides and sulfides for lithium–sulfur batteries, *Adv. Mater.*, 2017, **29**, 1601759.
9 J.-H. Zuo and Y.-J. Gong, Applications of transition-metal sulfides in the cathodes of lithium–sulfur batteries, *Tungsten*, 2020, **2**, 134–146.
10 S. J. Kim, K. Kim, J. Park and Y. E. Sung, Role and Potential of Metal Sulfide Catalysts in Lithium-Sulfur Battery Applications, *ChemCatChem*, 2019, **11**, 2373–2387.
11 P. Geng, *et al.*, Bimetallic metal-organic framework with high-adsorption capacity toward lithium Polysulfides for lithium–sulfur batteries, *Energy Environ. Mater.*, 2022, **5**, 599–607.
12 H. Park and D. J. Siegel, Tuning the adsorption of polysulfides in lithium–sulfur batteries with metal–organic frameworks, *Chem. Mater.*, 2017, **29**, 4932–4939.
13 L. W. Martin and A. M. Rappe, Thin-film ferroelectric materials and their applications, *Nat. Rev. Mater.*, 2016, **2**, 1–14.
14 K. Xie, *et al.*, Ferroelectric-enhanced polysulfide trapping for lithium–sulfur battery improvement, *Adv. Mater.*, 2017, **29**, 1604724.
15 T. Yim, *et al.*, Effective polysulfide rejection by dipole-aligned BaTiO3 coated separator in lithium–sulfur batteries, *Adv. Funct. Mater.*, 2016, **26**, 7817–7823.
16 R. Saroha, *et al.*, Asymmetric separator integrated with ferroelectric-BaTiO3 and mesoporous-CNT for the reutilization of soluble polysulfide in lithium-sulfur batteries, *J. Alloys Compd.*, 2022, **893**, 162272.
17 T. Kimura, *Molten salt synthesis of ceramic powders*, 2011.
18 M. Acosta, *et al.*, BaTiO3-based piezoelectrics: Fundamentals, current status, and perspectives, *Appl. Phys. Rev.*, 2017, **4**, 041305.
19 Y. Wang, *et al.*, Piezo-catalysis for nondestructive tooth whitening, *Nat. Commun.*, 2020, **11**, 1328.
20 M. Sharma, G. Madras and S. Bose, Process induced electroactive β-polymorph in PVDF: effect on dielectric and ferroelectric properties, *Phys. Chem. Chem. Phys.*, 2014, **16**, 14792–14799.
21 A. Hu, *et al.*, Optimizing redox reactions in aprotic lithium–sulfur batteries, *Adv. Energy Mater.*, 2020, **10**, 2002180.
22 Y. Zhou, *et al.*, Flower-like $Bi_4Ti_3O_{12}$/Carbon nanotubes as reservoir and promoter of polysulfide for lithium sulfur battery, *J. Power Sources*, 2020, **453**, 227896.
23 C. Chang, *et al.*, Molten salt assisted fabrication of ferroelectric BaTiO3 based cathode for high-performance lithium sulfur batteries, *Chem. Eng. J.*, 2022, **435**, 135031.
24 S. Zhang, *et al.*, A conductive/ferroelectric hybrid interlayer for highly improved trapping of polysulfides in lithium–sulfur batteries, *Adv. Mater. Interfaces*, 2019, **6**, 1900984.
25 N. Xu, *et al.*, Greatly suppressed shuttle effect for improved lithium sulfur battery performance through short chain intermediates, *Nano Lett.*, 2017, **17**, 538–543.
26 M. U. Patel, *et al.*, Li-S Battery Analyzed by UV/Vis in *Operando* Mode, *ChemSusChem*, 2013, **6**, 1177–1181.
27 J. Liu, *et al.*, Molecularly imprinted polymer enables high-efficiency recognition and trapping lithium polysulfides for stable lithium sulfur battery, *Nano Lett.*, 2017, **17**, 5064–5070.

28 Y. Pan, *et al.*, Polysulfides immobilization and conversion by nitrogen-doped porous carbon/graphitized carbon nitride heterojunction for high-rate lithium-sulfur batteries, *Electrochim. Acta*, 2022, **423**, 140387.
29 R. Müller, *et al.*, *Operando* Radiography and Multimodal Analysis of Lithium–Sulfur Pouch Cells—Electrolyte Dependent Morphology Evolution at the Cathode, *Adv. Energy Mater.*, 2022, **12**, 2103432.
30 W. Deng, Z. Xu, Z. Deng and X. Wang, Enhanced polysulfide regulation via honeycomb-like carbon with catalytic MoC for lithium–sulfur batteries, *J. Mater. Chem. A*, 2021, **9**, 21760–21770.
31 G. Janz, E. Roduner, J. Coutts and J. Downey, Raman studies of sulfur-containing anions in inorganic polysulfides. Barium trisulfide, *Inorg. Chem.*, 1976, **15**, 1751–1754.
32 L. Ma, *et al.*, A separator modified by barium titanate with macroscopic polarization electric field for high-performance lithium–sulfur batteries, *Nanoscale*, 2023, **15**, 5899–5908.
33 G. Kresse and J. Furthmüller, Efficiency of ab-initio total energy calculations for metals and semiconductors using a plane-wave basis set, *Comput. Mater. Sci.*, 1996, **6**, 15–50.
34 G. Kresse and J. Furthmüller, Efficient iterative schemes for ab initio total-energy calculations using a plane-wave basis set, *Phys. Rev. B: Condens. Matter Mater. Phys.*, 1996, **54**, 11169.
35 P. E. Blöchl, Projector augmented-wave method, *Phys. Rev. B: Condens. Matter Mater. Phys.*, 1994, **50**, 17953.
36 G. Kresse and D. Joubert, From ultrasoft pseudopotentials to the projector augmented-wave method, *Phys. Rev. B: Condens. Matter Mater. Phys.*, 1999, **59**, 1758.
37 J. P. Perdew, K. Burke and M. Ernzerhof, Generalized gradient approximation made simple, *Phys. Rev. Lett.*, 1996, **77**, 3865.
38 V. I. Anisimov, J. Zaanen and O. K. Andersen, Band theory and Mott insulators: Hubbard U instead of Stoner I, *Phys. Rev. B: Condens. Matter Mater. Phys.*, 1991, **44**, 943.
39 A. J. Cohen, P. Mori-Sánchez and W. Yang, Insights into current limitations of density functional theory, *Science*, 2008, **321**, 792–794.
40 S. L. Dudarev, G. A. Botton, S. Y. Savrasov, C. Humphreys and A. P. Sutton, Electron-energy-loss spectra and the structural stability of nickel oxide: An LSDA+ U study, *Phys. Rev. B: Condens. Matter Mater. Phys.*, 1998, **57**, 1505.
41 H. J. Monkhorst and J. D. Pack, Special points for Brillouin-zone integrations, *Phys. Rev. B: Solid State*, 1976, **13**, 5188.
42 N. Cadmen, J. Bustamante, R. Rivera, F. J. Torres and J. Ontaneda, Dopamine Adsorption on Rutile TiO2 (110): Geometry, Thermodynamics, and Core-Level Shifts from First Principles, *ACS Omega*, 2022, **7**, 4185–4193.
43 Q. T. Trinh, K. Bhola, P. N. Amaniampong, F. Jerome and S. H. Mushrif, Synergistic application of XPS and DFT to investigate metal oxide surface catalysis, *J. Phys. Chem. C*, 2018, **122**, 22397–22406.